Nano Research

Open Access

Research Article

Enhancing Li tolerance via Ag doping in high-efficiency CZTSSe solar cells

Yue Liu, Rutao Meng, Jiabin Dong, Han Xu, Xuejun Xu, Zixiu Cao, Jincheng Zhang, Haoran Li, and Yi Zhang

Institute of Photoelectronic Thin Film Devices and Technology, State Key Laboratory of Photovoltaic Materials and Cells, and Engineering Research Center of Thin Film Optoelectronics Technology, Ministry of Education, Nankai University, Tianjin 300350, China

Cite this article: *Nano Research*, **2025**, *18*, 94907337. https://doi.org/10.26599/NR.2025.94907337

ABSTRACT: Element doping has been widely recognized as an important strategy for improving the power conversion efficiency (PCE) of kesterite (CZTSSe) solar cells. Single-element doping has demonstrated substantial improvements in device performance. Therefore, multi-element doping strategies, utilizing the unique properties of individual dopants, have recently attracted significant attention. However, most of co-doping studies predominantly focused on the individual effects of doping elements on CZTSSe thin films, often overlooking the potential interactions between co-doping elements, thus limiting the development of the solar cells. In this study, we systematically investigated the optimal concentration of Li–Ag co-doping strategy and discovered that the incorporation of Ag effectively enhanced the thin film tolerance to higher Li doping concentration. The formation of dense upper grains following Ag doping suppressed the rapid Se diffusion rate during the initial reaction stages, thereby mitigating the deterioration of thin-film quality induced by excessive Li doping which is often considered to deteriorate the PCE of CZTSSe solar cells. Through precise control of doping concentrations (8% Li and 5% Ag), we achieved a remarkable PCE of 13.42%. This study underscores the critical importance of considering dopant interactions in multi-element doping strategies, providing new insights for the development of thin film solar cells.

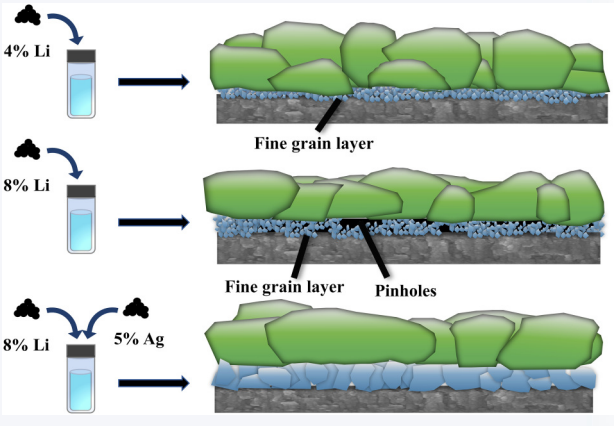

KEYWORDS: Li–Ag co-doping, Li tolerance, grain growth, thin film solar cells

1 Introduction

Kesterite (CZTSSe) thin film has drawn considerable attention due to its excellent photovoltaic characteristics in recent years [1–3]. The earth-abundant and non-toxic constituents make it a promising candidate to replace the traditional Cu(In,Ga)Se_2 (CIGS) or CdTe thin film solar cells. Recently, the power conversion efficiency (PCE) of the kesterite-based thin film solar cells has achieved substantial breakthrough to 15.1% [4]. However, it is still far below the Shockley–Queisser limit and the requirement of large-scale commercial application [5, 6]. The primary reason impeding the further development of kesterite thin film solar cells is the severe open circuit voltage (V_{OC}) deficit ($V_{OC,def} = E_g/q - V_{OC}$) caused by undesirable film quality and detrimental defects [7, 8]. Therefore, a variety of strategies, such as elements doping [9–13], interface passivation [14–16], and post-annealing treatment [2, 14, 17–19], have been utilized to effectively decouple the sources of V_{OC} deficit.

Doping with elements such as alkali elements, Ag [20, 21], Cd [22, 23], Ge [24–26] has consistently proven to be an effective strategy for mitigating the V_{OC} deficit and enhancing PCE of CZTSSe solar cells. The selenides of the doping elements can effectively facilitate the interdiffusion of the constituents and passivate the formation of detrimental secondary phases during the high-temperature annealing process. Besides, due to the occupation of certain lattice sites, the formation of harmful defects related to Cu, Zn, or Sn will also be suppressed. Among the various doping elements, Li and Ag have emerged as the most extensively utilized, even becoming fundamental components in some studies [20, 27–29]. Zhang et al. found that Li-doping could effectively improve the quality of the absorber thin film, eliminate the bottom fine grain layer, suppress detrimental defects, and optimize the band alignment at the CdS interface [11]. Cheng et al. introduced Li into

Received: February 7, 2025; **Revised:** February 25, 2025
Accepted: February 26, 2025

Address correspondence to yizhang@nankai.edu.cn

the flexible CZTSSe solar cells, resulting in enhanced carrier transport and reduced carrier recombination [30]. Similar to Li doping, Ag doping has also been demonstrated to facilitate phase evolution, improve thin film quality, and passivate detrimental defects [31, 32]. It needs to be indicated that Ag tends to preferentially occupy Cu lattice sites during the selenization process, while Li prefers to segregate at grain boundaries [9, 33]. This distinct behavior results in slightly different mechanisms for the improvement of the device performance. As a result, the co-doping strategy, which combines the complementary effects of both elements, has been explored and widely adopted in current studies [34–36]. For example, Wu et al. successfully achieved a high fill factor (FF) of 74.30% for Li–Ag co-doped CZTSSe solar cells [28], while Saucedo et al. also achieved PCE over 14% by implementing Li and Ag co-doping in CZTSSe solar cells [37].

However, it is noteworthy that most current studies on Li–Ag co-doping strategy are all neglect the potential dopant interactions. Specifically, they do not consider whether the additional new element would alter or interfere with the performance of previously introduced dopants and which could in fact suppress the PCE development of solar cells. In this study, we employed a co-doping method by using Ag and Li to enhance the PCE of the CZTSSe solar cells. During the investigation of different doping concentrations, we found that while high-concentration Li doping demonstrated an effective enhancement in V_{OC}, the worsening thin film quality because of the excess Li dopant leads to substantial degradation in both short-circuit current density (J_{SC}) and FF. The incorporation of Ag facilitated the formation of a denser surface layer during the initial selenization stage, effectively suppressing the rapid Se diffusion into the absorber layer under excessive Li-doping. This surface modification effectively modulates the reaction kinetics of the thin film and suppresses the formation of the thick fine grain layer. With the introduction of Ag, the optimal Li-doping concentration increased to 8%, doubling the value when Li was doped alone. As a result, due to the enhanced film quality, the co-doped CZTSSe solar cells achieved a notable PCE of 13.42% at optimal doping concentrations of 8% Li and 5% Ag.

2 Results and discussion

Figure 1(a) illustrates the structure of the CZTSSe solar cell in this study, which includes glass substrate, Mo back electrode, CZTSSe absorber layer, CdS buffer layer, intrinsic zinc oxide (i-ZnO)/aluminum-doped zinc oxide (AZO) window layers, and Ag grid electrodes. The process of achieving Li and Ag co-doping in this work is illustrated in Fig. 1(b). LiCl and AgCl powders were directly dissolved into the precursor solution. Subsequently, the Cu_2ZnSnS_4 (CZTS) precursor film was prepared through spin-coating followed by pre-annealing. Finally, the Li–Ag co-doped CZTSSe absorber layer was obtained after the high-temperature selenization process.

Before exploring the co-doping mechanism of Li and Ag, we first investigated the impact of single Li doping on the performance of CZTSSe solar cells, and the device parameters are shown in Fig. S1 in the Electronic Supplementary Material (ESM). The photovoltaic parameters of the devices were significantly improved after Li doping. This is consistent with the results of our previous studies [9, 11, 38]. As the Li doping concentration is 4%, the PCE of the solar cell reaches its maximum value (11.79%). As the Li concentration increases further, the V_{OC} continues to rise, but both the FF and J_{SC} decrease sharply, leading to an overall decline in PCE of device. To elucidate the underlying mechanism of this phenomenon, morphological characterization of the absorber layer under different Li doping concentrations was conducted through surface and cross-sectional scanning electron microscopy (SEM). As shown in Fig. S2 in the ESM, the incorporation of 4% Li effectively enhances the quality of thin films. The fine grain layer, which could impede the transport of photogenerated carriers in the back region and significantly increase the series resistance [39], is effectively reduced. However, as the Li concentration is further increased, a corresponding expansion of the fine grain layer thickness is observed. Additionally, the film surface exhibits an increased density of pinholes, which also leads to the deterioration of the device performance. While excessive Li doping is found to enhance the V_{OC}, it simultaneously induces degradation of film quality, adversely affecting both the FF and J_{SC}. This ultimately results in a reduction of PCE. Figure S3 in the ESM shows the X-ray diffraction (XRD) result of CZTSSe thin films under different Li doping concentrations, and no secondary phases are detected. Since the covalent bond radius of Li–Se is 1.33 Å while that of Cu–Se is 1.27 Å, if Li substitutes for the Cu site, the XRD diffraction peak would shift toward lower angles. However, upon magnifying the (112) peak of the obtained XRD data (Fig. S3(b) in the ESM), no shift in the peak position is observed, which indicates that Li does not incorporate into the lattice.

The incorporation of 4% Li significantly improves the performance of CZTSSe solar cells, yielding a maximum PCE of 11.79%. However, the V_{OC} of the solar cells still remains

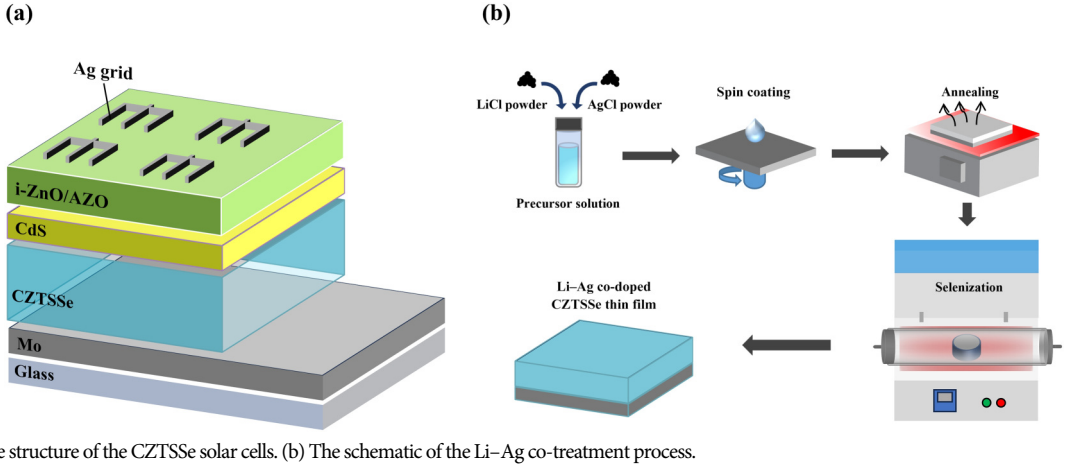

Figure 1 (a) The structure of the CZTSSe solar cells. (b) The schematic of the Li–Ag co-treatment process.

undesirable, suggesting considerable potential for the improvement. Therefore, we implemented a further optimization strategy through the introduction of Ag as an additional dopant. To determine the optimal co-doping concentrations of Ag and Li, we employed nine different concentration combinations of 4% Li + 5% Ag, 4% Li + 10% Ag, 4% Li + 15% Ag, 8% Li + 5% Ag, 8% Li + 10% Ag, 8% Li + 15% Ag, 12% Li + 5% Ag, 12% Li + 10% Ag, and 12% Li + 15% Ag, and the performances of these devices are shown in Fig. 2(a) and Fig. S4 in the ESM. To provide a more intuitive representation of the changes in the performances of the solar cells, we systematically calculated the average parameter values and generated a comprehensive contour map to illustrate the spatial distribution of device characteristics, as shown in Fig. 2(b) and Fig. S5 in the ESM. The synergistic incorporation of Ag with Li leads to a remarkable enhancement in photovoltaic performance, achieving a highest average PCE of 12.090% at doping concentrations of 8% Li and 5% Ag. When the Ag concentration exceeds the optimal level, the device performance begins to degrade. The FF shows a similar improvement with PCE, while the change of V_{OC} exhibits completely opposite trends to the J_{SC}. The V_{OC} shows a consistent increase with rising Li and Ag concentrations, similar to the effect observed from Li doping alone, while J_{SC} gradually declines.

Compared to Li doping alone, the introduction of Ag increases the optimal concentration of Li to 8%, two times the previous value.

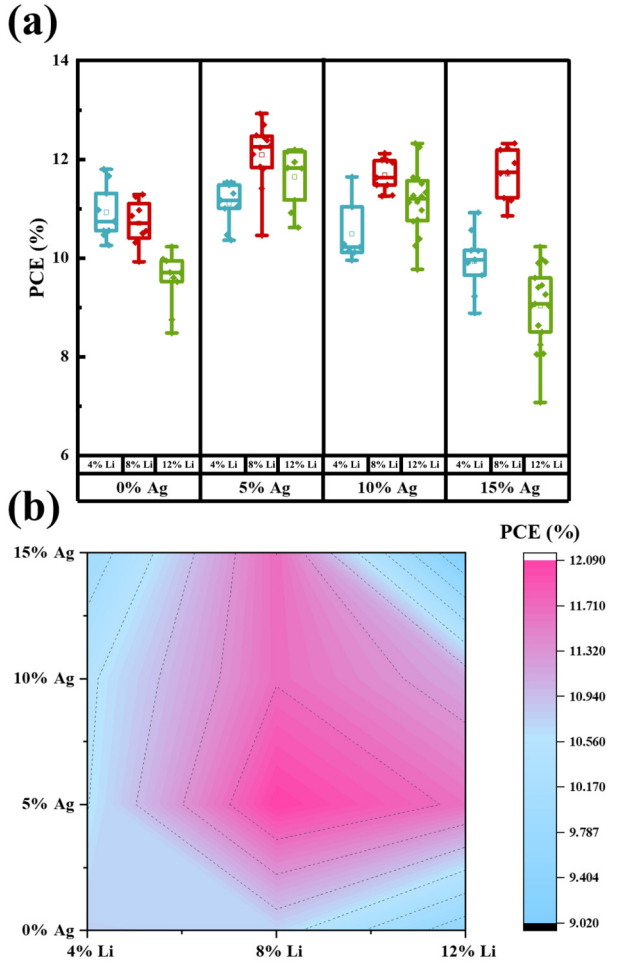

Figure 2 (a) The PCE of the CZTSSe solar cells under different Li and Ag doping concentrations. (b) The contour map of the average PCE of the CZTSSe solar cells under different Li and Ag doping concentrations.

This attractive phenomenon prompts us to investigate the underlying mechanisms by analyzing the changes in both the photoelectrical properties and thin film morphology. The external quantum efficiency (EQE) measurement was first conducted to investigate the impact of different doping concentrations on the light response. The optical band gaps of the thin films under different doping concentrations were also calculated based on EQE spectra. Figure S6 in the ESM shows the results of EQE measurement and the calculated optical bandgap. The EQE spectra reveal a notable decrease in the long-wavelength region with increasing doping concentration, which is directly correlated with the observed reduction in J_{SC}. Furthermore, the contour mapping analysis presented in Fig. 3(a) demonstrates a consistent widening of the optical bandgap with elevated Ag concentrations, also providing an explanation for both the decreased J_{SC} and enhanced V_{OC}. Besides, we find that the variation in the optical bandgap of the thin film appears to have little correlation with the Li content. The maximum variation in the bandgap induced by changes in Li content is negligibly 0.015 eV, which further indicates that most of the doped Li tends to accumulate at the grain boundaries rather than substitutes Cu sites. In contrast, the introduction of Ag significantly increases the bandgap from 1.077 to 1.154 eV, indicating that Ag could substitute the Cu sites and result in a more significant impact on the bandgap. Except for EQE, the capacitance–voltage (C–V) measurement was also carried out to investigate the changes in depletion region widths and carrier density (N_{CV}) under different doping concentrations, as shown in Fig. S7 in the ESM. Figures 3(b) and 3(c) show the contour maps of the calculated depletion region widths and N_{CV}. In the absence of Ag doping, the increase in Li concentration leads to a significant reduction in the depletion region widths. While the N_{CV} increases significantly, the small depletion region width can hinder the collection of the photo-generated carriers, resulting in lower J_{SC} [40]. The introduction of Ag could effectively enhance the depletion region widths and promote the carrier collection efficiency. However, the low N_{CV} under high Ag-doping concentration also reduces the formation of photo-generated carriers, thereby deteriorating the device performance.

Although the EQE and C–V measurements partially explain the reasons for the variations in the device parameters, especially the J_{SC} and V_{OC}, the results show a linear dependence on both Li and Ag concentrations, making it difficult to explain why the optimal PCE occurs at 8% Li + 5% Ag. Therefore, we further investigated the impact of different doping concentrations on the quality of CZTSSe thin films by using SEM. As shown in Fig. S8 in the ESM, the surface quality of the absorber layer exhibits a significant improvement following the additional Ag doping. Due to the enhanced growth-assisting effect of Ag, the surface morphology becomes denser and more compact, while the grain size also experiences a substantial increase. When the concentrations of Li and Ag are excessively high, a considerable number of voids are observed on the surface of the thin film. These voids may act as shunt paths, impeding carrier transport and thus degrading the FF of the device [41]. Furthermore, as the CdS buffer layer is deposited using the chemical bath deposition (CBD) method, these voids may facilitate the infiltration of the solution, potentially leading to the detachment of the thin film. The cross-sectional SEM images of the absorber layers are shown in Fig. 4. Although the introduction of Ag does not eliminate the double layer structure of the absorber layer, it significantly enhances the crystallization at the back

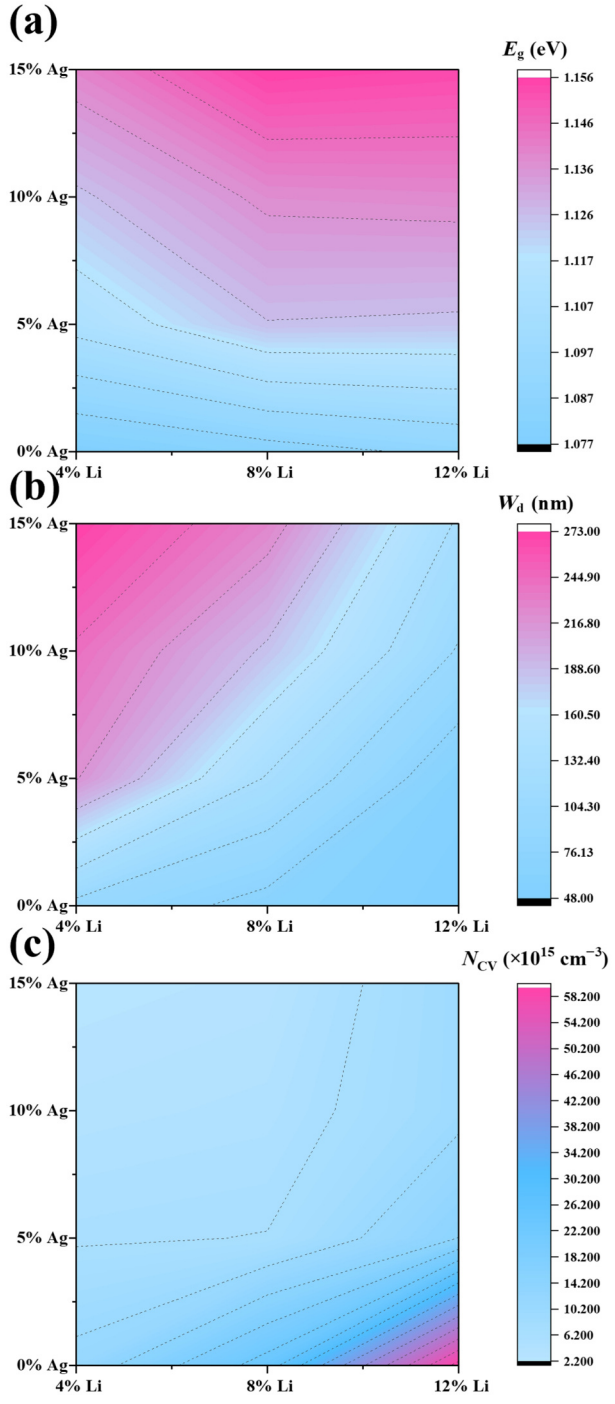

Figure 3 The contour maps of (a) optical band gap, (b) depletion region widths, and (c) carrier density for CZTSSe solar cells under different Li and Ag doping concentrations.

interface and transforms the fine fragments to small crystals. This also explains the reason why the FF of CZTSSe solar cells is significantly promoted after the Ag doping. In addition to the surface morphology, excessive doping concentration of Ag also results in the formation of large voids at the bottom of the absorber layer. The presence of these voids not only impedes carrier transport to the back electrode, but also weakens the adhesion between the film and the Mo substrate, making the thin films more susceptible to detachment during subsequent processing steps [42]. Both cross-sectional and surface SEM analyses reveal that the quality of absorber layer is the best at 8% Li and 5% Ag doping concentrations. Therefore, although the electrical performance is not the best under these doping concentrations, the PCE of CZTSSe solar cells reaches the maximum.

Above all, the introduction of Ag not only optimizes the electrical properties of the CZTSSe thin film, but also, more importantly, substantially improves the quality of the absorber layer. This enhancement results in an increased tolerance to doped Li content in the film, with the optimal Li doping concentration rising to 8%. To further investigate the impact of Ag doping on the film growth under high-concentration Li doping, we conducted an interruption experiment to investigate the thin film growth at each stage. For clearer distinction in future discussions, the samples used in the interruption experiments are referred to as the "sample W/O" for the sample doped with 8% Li and the "sample W/" for the sample co-doped with 8% Li and 5% Ag. The annealing temperature ramp curve for this work is shown in Fig. S9 in the ESM. To systematically investigate the growth mechanism of the thin films, we select five distinct temporal stages of the selenization process: (A) precursor stage (0 s), (B) pre-selenization stage (360 s), (C) initial selenization stage (610 s), (D) intermediate selenization stage (1090 s), and (E) final selenization stage (1570 s). Comprehensive characterization was performed on the sample prepared at each stage, including surface and cross-sectional SEM analysis to monitor morphological changes, complemented by XRD and Raman measurements to track phase evolution. Figure S10 in the ESM presents the morphological characteristics of precursor thin films for both samples W/ and W/O. The Ag-doped precursor layer exhibits a denser surface with fewer cracks, suggesting that Ag incorporation facilitates partial crystallization even during the low-temperature annealing process at 290 °C in the spin-coating stage, resulting in a more compact and homogeneous precursor thin film. In contrast to the surface morphology differences, cross-sectional SEM shows negligible variation between the samples W/ and W/O. The XRD patterns and Raman spectra also show no significant differences, and only the phase related to CZTS is detected [43]. Figure S11 in the ESM presents the surface and cross-sectional images of the thin films after pre-selenization at 350 °C for 5 min. The surface morphology shows numerous small islands on the surface of the thin films, which can serve as nucleation centers during the subsequent high-temperature selenization process and thus enhance thin film growth quality. Notably, the Ag-doped sample exhibits larger surface islands, providing further evidence that Ag effectively facilitates film growth even under low-temperature conditions. Due to the relatively low processing temperature, the reactions are predominantly conducted at the surface level, leading to the negligible changes in the cross-sectional morphologies of the thin films. As for Raman and XRD measurements, the surface-sensitive Raman spectroscopy enables the detection of CZTSSe phase formation, whereas XRD shows no substantial changes of both thin films [44].

Figure 5 presents the surface and cross-sectional SEM morphologies of the films at the early stages of the high-temperature selenization process. At this stage, both samples exhibit the formation of relatively large grains on their surfaces. However, in comparison to the Ag-doped sample, the sample W/O features smaller grains and an increased density of voids on the surface. Cross-sectional images of these two samples also reveal that the incorporation of Ag leads to the formation of a denser layer on the

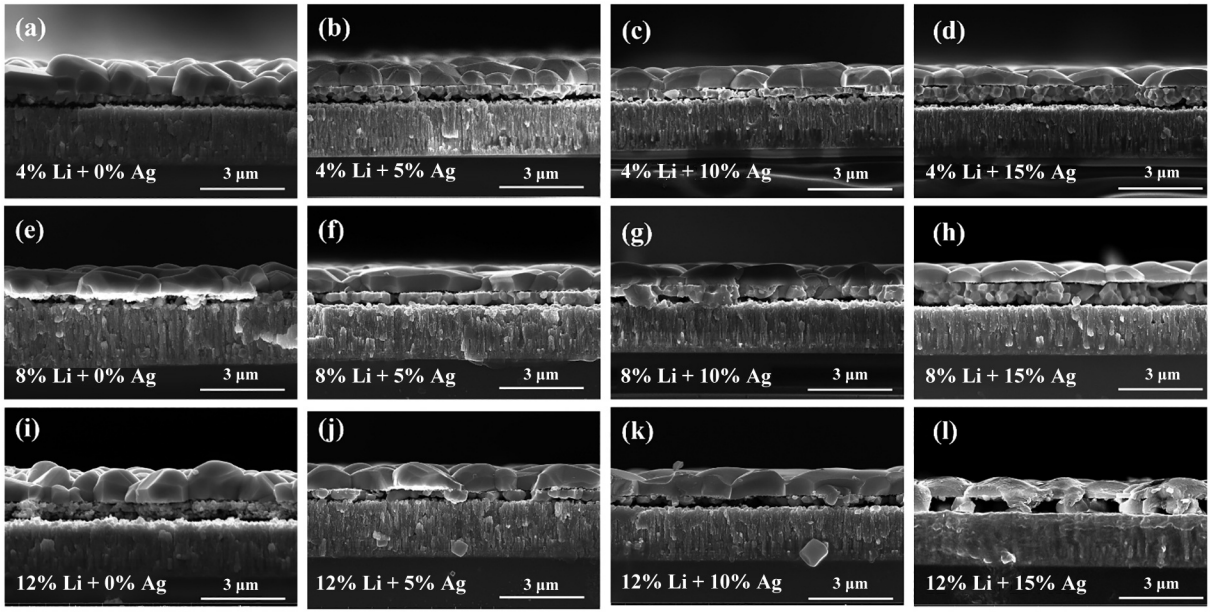

Figure 4 The cross-sectional SEM images of the CZTSSe absorber layers under different Li and Ag doping concentrations. The specific doping concentration of the thin films is labeled at the bottom left corner of each image.

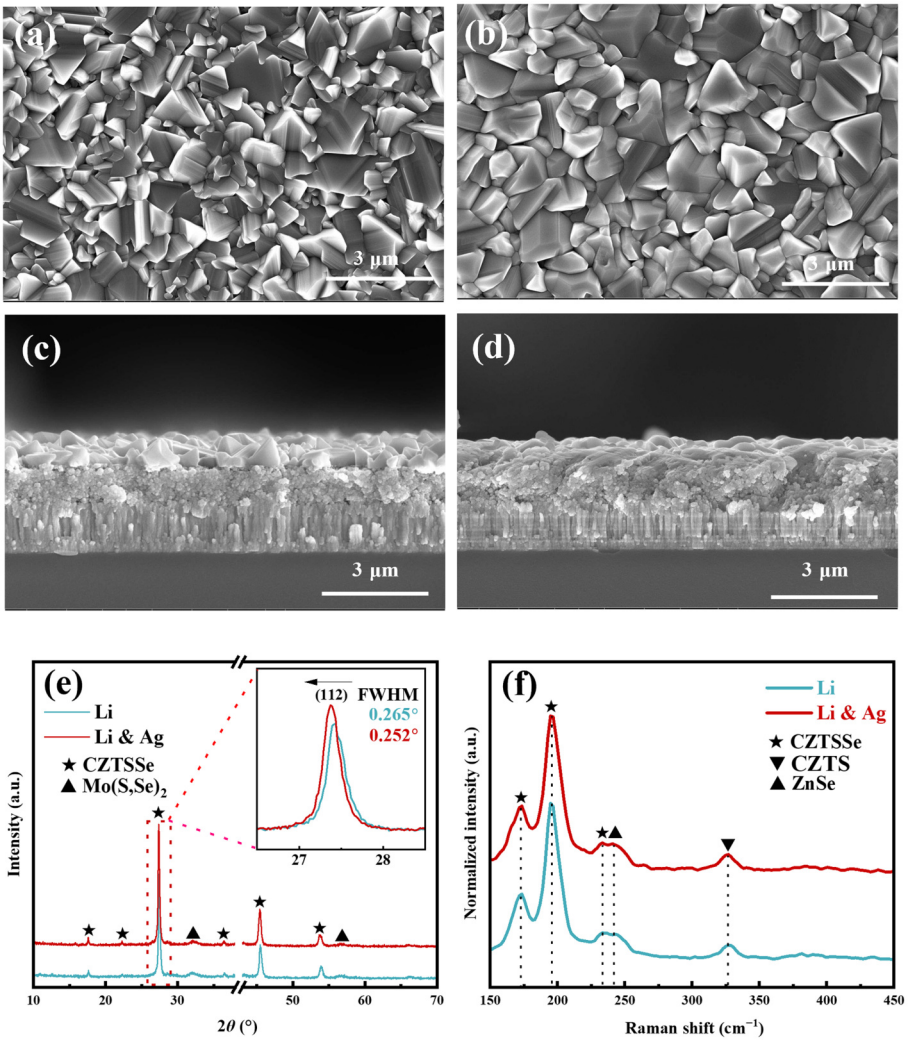

Figure 5 The surface and cross-sectional SEM images of the ((a) and (c)) sample W/O and ((b) and (d)) sample W/ at the interruption point C. (e) XRD patterns and (f) Raman spectra of the two samples at the interruption point C.

surface of the thin film. In contrast, the Li-doped sample exhibits a sparse grain structure near the surface, which fails to provide complete coverage across the entire film surface. As the phase transition initiates during the high temperature annealing process, significant changes are observed in both the XRD patterns and Raman spectra. The three strongest diffraction peaks located at 27°, 46°, and 54° can be indexed to the (112), (204), and (312) planes of CZTSSe [45]. After amplifying the (112) peaks of the two samples, a shift toward a lower angle is observed in the W/ sample, confirming the successful incorporation of Ag into the CZTSSe lattice. Furthermore, the calculated full width at half maximum (FWHM) of the (112) peak is 0.265° for the sample W/O and 0.252° for the sample W/, suggesting that the co-doped film exhibits higher crystallinity. This observation indicates that during the early stages of the selenization process, the incorporation of Ag accelerates the reaction kinetics in the co-doped sample, thereby enhancing the crystallinity of the film. In the Raman spectra, the peaks located at 173, 196, and 234 cm^{-1} correspond to the B mode, A mode, and E mode of CZTSSe, respectively [46]. No secondary phases are detected except for ZnO, which can be attributed to the Zn-rich solution used in the precursor synthesis process.

As the reaction enters into the middle stage of the selenization process, the growth of the upper layer of the film is nearly complete, as shown in Fig. 6. The incorporation of Ag leads to the formation of larger and more compact grains in the upper layer of the sample W/, which is consistent with the early stage. Cross-sectional SEM images reveal that sample W/ displays a structure consisting of large grains in the upper layer and small grains in the bottom layer, while the sample W/O shows a thicker fine grain layer at the bottom. The XRD patterns at this stage show significant changes compared to those observed in the early stage. After calculating the FWHM of the enlarged (112) peaks for these two samples, we find that the sample W/O exhibits a smaller FWHM compared to that of the sample W/, which is in complete contrast to the results obtained at the previous interruption points. Based on the morphologies of the sample W/O shown in Fig. 5, we speculate that the excessively sparse upper-layer structure in the sample W/O facilitates the formation of selenium diffusion channels. Since Li is known to promote the interdiffusion of Se, high concentration of Li further accelerates the reaction rate during the middle stages of the selenization process. Figure S12 in the ESM compares the XRD intensities of $Mo(S,Se)_2$ peaks observed in samples W/ and W/O during the early and middle stages of the selenization process. It is shown that the peak intensity of $Mo(S,Se)_2$ for the sample W/O is consistently higher than that of the sample W/, suggesting that a great amount of Se diffuses to the back interface and reacts with Mo

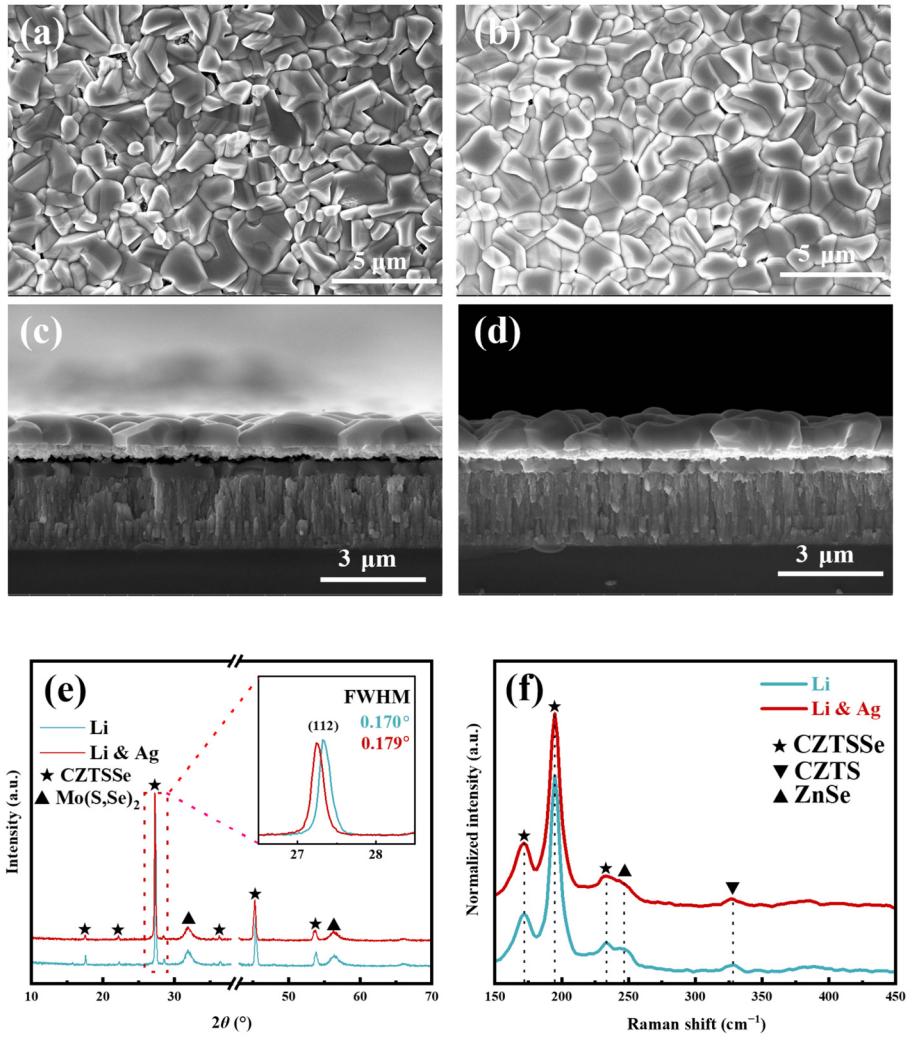

Figure 6 The surface and cross-sectional SEM images of the ((a) and (c)) sample W/O and ((b) and (d)) sample W/ at the interruption point D. (e) XRD and (f) Raman spectra of the two samples at the interruption point D.

substrate. As for sample W/, the more compact upper grain structure induced by Ag doping helps to regulate the diffusion rate of Se to some extent. As a result, the phase transition speed in the sample W/O surpasses that in the sample W/ during the middle reaction stage. Although the rapid diffusion of Se facilitates film growth, the excessive diffusion of Se can also lead to the formation of a large number of fine grains at the bottom layer, resulting in degradation of the overall film quality and adversely affecting the efficiency of the device. From the Raman results, the three peaks representing CZTSSe continue to rise, while the peaks of CZTS show a significant decrease. No secondary phases except for ZnSe are observed.

At the end of the selenization process, due to the critical role of the Ag incorporation in regulating the diffusion rate of Se, the formation of the fine grain layer at the bottom is effectively controlled. As shown in Fig. 7, more compact and denser morphologies are observed in both the surface and cross-sectional SEM images for sample W/. Besides, the FWHM calculated from XRD for the samples W/ and W/O are 0.152° and 0.156°, respectively. The thin film quality of the sample W/ surpasses that of the sample W/O. Figure S13 in the ESM more intuitively shows the FWHM changes of samples W/O and W/ under different reaction stages. In the middle and early stages of the reaction, the phase transition rate of sample W/O is significantly faster than that of sample W/, thereby confirming our hypothesis that Ag doping helps control the reaction rate during the film growth and improve the final quality of the CZTSSe thin film. In the Raman spectra, the peak corresponding to CZTS has almost disappeared, indicating that the phase transformation from CZTS to CZTSSe has completed. Furthermore, no other secondary phases are observed throughout the reaction process, suggesting that the addition of Ag primarily enhances the quality of the film by optimizing the bottom fine grain layer.

Finally, due to the substantial enhancement in the film quality, the PCE for CZTSSe solar cells increases from 10.29% for undoped sample to 12.93% with 8% Li and 5% Ag co-doping, as shown in Fig. 8. After the application of a MgF_2 anti-reflective layer, the device efficiency is further enhanced, reaching 13.42% (Fig. S14 in the ESM). Table S1 in the ESM summarizes the detailed parameters of Li–Ag co-doped CZTSSe solar cells in this study, along with device parameters from recent studies on Li and Ag doping. By optimizing the doping concentrations of Li and Ag, we have achieved relatively advanced performance in terms of PCE and V_{OC} compared to those in other studies. More importantly, most previous studies were conducted based on the optimal doping concentration of a single element, overlooking the impact of

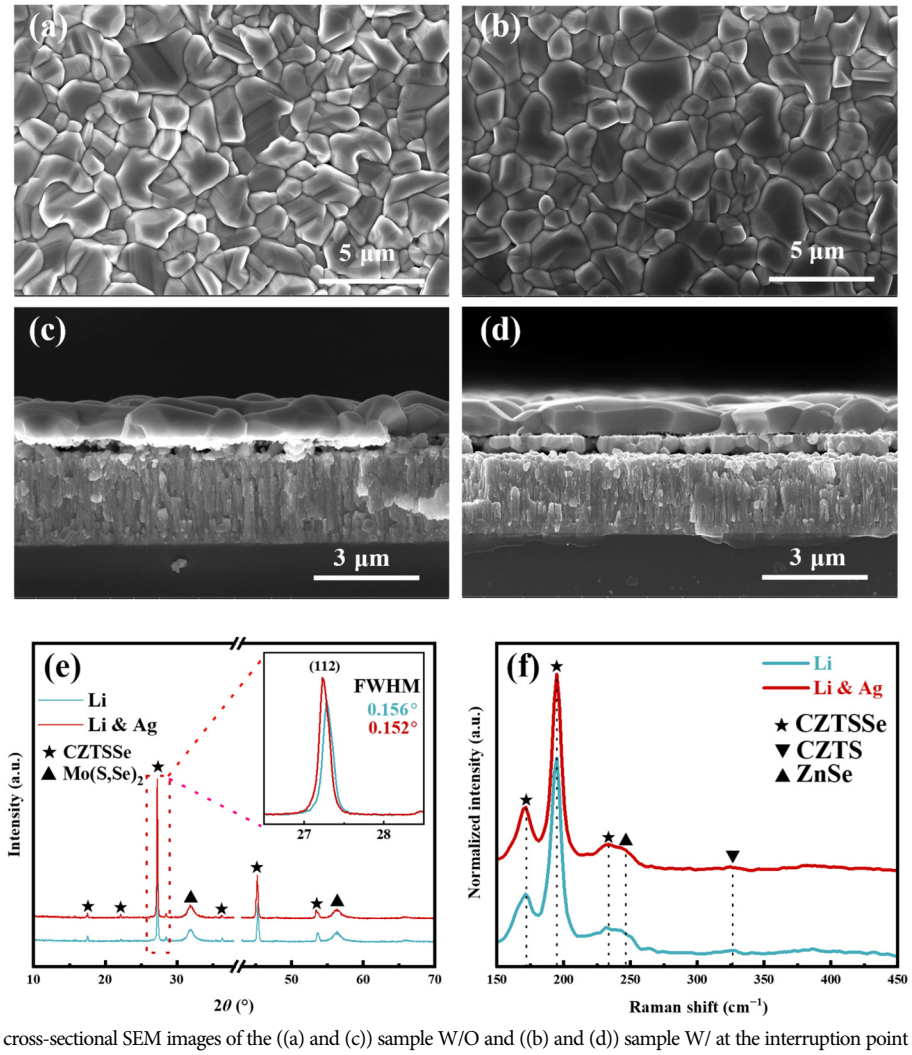

Figure 7 The surface and cross-sectional SEM images of the ((a) and (c)) sample W/O and ((b) and (d)) sample W/ at the interruption point E. (e) XRD patterns and (f) Raman spectra of the two samples at the interruption point E.

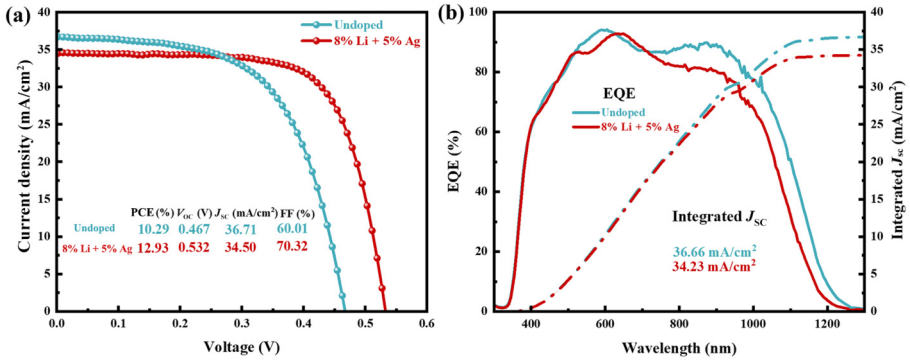

Figure 8 (a) *J*–*V* and (b) EQE curves of the undoped sample and the sample doped with 8% Li and 5% Ag.

additional elements on the previously incorporated dopants. This study highlights the significance of considering these interactions in multi-element co-doping to achieve optimal performance. Besides, after over two months of storage in the atmospheric environment without encapsulation, the PCE of the solar cell shows almost no significant degradation, as shown in Table S2 in the ESM, demonstrating its excellent stability.

3 Conclusion

In this work, we investigate the optimal doping concentrations for Li and Ag co-doping and find that the incorporation of Ag significantly enhances the tolerance to the Li doping concentration in the CZTSSe film. Li doping can effectively enhance the performance of the solar cell. However, when the Li concentration reaches a certain level, the increased number of voids on the film surface and the excessively thick fine grain layer at the back interface lead to decreases of FF and J_{SC} for the solar cell, thereby affecting the overall device efficiency. With the addition of Ag, its strong growth-assisting effect leads to the formation of a denser grain layer on the surface at the early stages of selenization process. This dense layer effectively controls the diffusion rate of Se, thereby suppressing the excessive formation of fine grain layer at the bottom. This effectively suppresses the deterioration of film quality caused by excessively high Li doping concentrations, resulting in a better performance of CZTSSe solar cells. As a result, the introduction of Ag significantly enhances the film's tolerance to Li concentration, nearly doubling its capacity, and achieves a PCE of 13.42% for CZTSSe solar cells with 8% Li and 5% Ag co-doping. This study establishes a valuable framework for future research on co-doping strategies involving various elements. The systematic investigation of dopant interactions and optimization of doping concentrations may pave the way for achieving higher PCE of solar cells.

4 Methods

4.1 Preparation of CZTSSe thin film

CZTSSe absorber thin films were prepared by sol-gel methods followed by selenization process. $Cu(CH_3COO)_2{\cdot}H_2O$ (Aladdin, 99.95%), $ZnCl_2$ (Aladdin, 99.99%), $SnCl_2{\cdot}2H_2O$ (Aladdin, 99.99%), and thiourea (Bohai Chem, 99%) were dissolved into the N,N-dimethylformamide (Macklin, 99%) to obtain the precursor solution. Li and Ag doping were achieved by directly incorporating LiCl (Aladdin, 99.99%) and AgCl (Macklin, 99.9%) powders into the precursor solution. The molar ratios of Li/(Ag + Cu) were set at 4%, 8%, and 12%, while the molar ratios of Ag/(Ag + Cu) were set at 5%, 10%, and 15%. Upon complete dissolution of the solute, the precursor thin films were subsequently prepared by the spin-coating method on the Mo-coated soda-lime glass in a glovebox. Before the selenization process, an atomic layer deposition (ALD)-Al_2O_3 treatment was applied onto the surface of the precursor films, as described in our previous study [1]. Subsequently, the precursor films and 0.6 g Se powder were placed in a graphite box and annealed at 560 °C for 20 min in a rapid thermal processing (RTP) tube furnace to obtain the ideal absorber thin films.

4.2 Fabrication of CZTSSe solar cells

Following the preparation of the absorber thin films, a CdS buffer layer was deposited through CBD. Subsequently, 50 nm i-ZnO and 500 nm AZO layers were deposited via sputtering system. 500 nm Ag electrode was then deposited using thermal evaporation method. The active area of each CZTSSe solar cell was 0.185 cm^2. Finally, 80 nm MgF_2 anti-reflective layer was deposited on the solar cells with the highest PCE by using the thermal evaporation method.

Electronic Supplementary Material: Supplementary material (the PCE, SEM, and XRD data of the thin films doped with Li alone, the PCE, EQE, *C*–*V*, and SEM data of the thin films under different Li–Ag co-doping concentrations, the selenization temperature rise curve, the PCE, SEM, XRD, and Raman data of the thin films under Li–Ag co-doping and Li doping alone, and the PCE comparison of related works and test result of stability) is available in the online version of this article at https://doi.org/10.26599/NR.2025.94907337.

Data availability

All data needed to support the conclusions in the paper are presented in the manuscript and the ESM. Additional data related to this paper may be requested from the corresponding author upon request.

Acknowledgements

This work was supported by the National Key Research & Development Program of China (No. 2024YFB4205300).

Declaration of competing interest

All the contributing authors report no conflict of interests in this work.

Author contribution statement

Y. L.: Data curation, investigation, supervision, project administration, validation, writing – original draft, writing – review & editing. R. T. M. and J. B. D.: Data curation, investigation, writing – original draft. H. X.: Investigation, writing – original draft. X. J. X., Z. X. C., J. C. Z., and H. R. L.: Data curation, investigation. Y. Z.: Supervision, project administration, validation, resources, writing – original draft, writing – review & editing.

Use of AI statement

None.

References

[1] Wang, Z. Y.; Meng, R. T.; Guo, H. L.; Sun, Y. L.; Liu, Y.; Zhang, H. M.; Cao, Z. X.; Dong, J. B.; Xu, X. J.; Liang, G. X. et al. Toward high efficient $Cu_2ZnSn(S_x,Se_{1-x})_4$ solar cells: Break the limitations of V_{OC} and FF. *Small* **2023**, *19*, 2300634.

[2] Guo, H. L.; Meng, R. T.; Wang, G.; Wang, S. H.; Wu, L.; Li, J. J.; Wang, Z. Y.; Dong, J. B.; Hao, X. J.; Zhang, Y. Band-gap-graded $Cu_2ZnSn(S,Se)_4$ drives highly efficient solar cells. *Energy Environ. Sci.* **2022**, *15*, 693–704.

[3] Sun, Y. L.; Qiu, P. F.; Yu, W.; Li, J. J.; Guo, H. L.; Wu, L.; Luo, H.; Meng, R. T.; Zhang, Y.; Liu, S. Z. N-type surface design for p-type CZTSSe thin film to attain high efficiency. *Adv. Mater.* **2021**, *33*, 2104330.

[4] Green, M. A.; Dunlop, E. D.; Yoshita, M.; Kopidakis, N.; Bothe, K.; Siefer, G.; Hinken, D.; Rauer, M.; Hohl-Ebinger, J.; Hao, X. J. Solar cell efficiency tables (version 64). *Prog. Photovolt.* **2024**, *32*, 425–441.

[5] Buatong, N.; Tang, I. M.; Pon-On, W. The study of metal sulfide as efficient counter electrodes on the performances of CdS/CdSe/ZnS-co-sensitized hierarchical TiO_2 sphere quantum dot solar cells. *Nanoscale Res. Lett.* **2017**, *12*, 170.

[6] Zhou, J. Z.; Xu, X.; Wu, H. J.; Wang, J. L.; Lou, L. C.; Yin, K.; Gong, Y. C.; Shi, J. J.; Luo, Y. H.; Li, D. M. et al. Control of the phase evolution of kesterite by tuning of the selenium partial pressure for solar cells with 13.8% certified efficiency. *Nat. Energy* **2023**, *8*, 526–535.

[7] Kim, J.; Shin, B. Strategies to reduce the open-circuit voltage deficit in $Cu_2ZnSn(S,Se)_4$ thin film solar cells. *Electron. Mater. Lett.* **2017**, *13*, 373–392.

[8] Li, J. J.; Huang, Y. C.; Huang, J. L.; Liang, G. X.; Zhang, Y. X.; Rey, G.; Guo, F.; Su, Z. H.; Zhu, H. B.; Cai, L. L. et al. Defect control for 12.5% efficiency $Cu_2ZnSnSe_4$ kesterite thin-film solar cells by engineering of local chemical environment. *Adv. Mater.* **2020**, *32*, 2005268.

[9] Shen, Z.; Wang, S. Y.; Liu, Y.; Sun, Y. L.; Wu, J. Y.; Guo, H. L.; Zhang, K. Z.; Zhang, S. L.; Liu, F. F.; Zhang, Y. Li_2S doping into CZTSe drives the large improvement of V_{OC} of solar cell. *J. Energy Chem.* **2021**, *62*, 637–644.

[10] Sun, X. F.; Li, M. G.; Yao, B.; Li, Y. F.; Ding, Z. H.; Ma, D.; Sun, Y. T.; Zhu, Y.; Ding, N.; Shi, L. Y. et al. Enhancing the efficiency of CZTSSe solar cells by optimizing K-doping concentration and selenization temperature. *ACS Appl. Energy Mater.* **2025**, *8*, 1879–1886.

[11] Guo, H. L.; Wang, G.; Meng, R. T.; Sun, Y. L.; Wang, S. Y.; Zhang, S. L.; Wu, J. Y.; Wu, L.; Liang, G. X.; Li, H. et al. An efficient Li^+-doping strategy to optimize the band alignment of a $Cu_2ZnSn(S,Se)_4$/CdS interface by a Se&LiF co-selenization process. *J. Mater. Chem. A* **2020**, *8*, 22065–22074.

[12] Zhao, X. Y.; Li, J. R.; Hu, C. Y.; Qi, Y. F.; Zhou, Z. J.; Kou, D. X.; Zhou, W. H.; Yuan, S. J.; Wu, S. X. Revealing the role of hydrogen in highly efficient Ag-substituted CZTSSe photovoltaic devices: Photoelectric properties modulation and defect passivation. *Nano-Micro Lett.* **2025**, *17*, 84.

[13] Zheng, Y. Y.; Xiang, C. X.; Gong, Y. C.; Li, Y. Z.; Xiao, S. L.; Guo, H. Y.; Ma, C. F.; Wang, S. Y.; Yan, W. B.; Huang, W. et al. Effects of cadmium alloying on solution-processed CZTSSe solar cells: Morphology, band alignment and efficiency improvement. *Sci. China Mater.* **2025**, *68*, 523–530.

[14] Wang, S. Y.; Shen, Z.; Sun, Y. L.; Li, H.; Zhang, K. Z.; Wu, L.; Ao, J. P.; Zhang, Y. Defects and surface electrical property transformation induced by elemental interdiffusion at the p–n heterojunction via high-temperature annealing. *ACS Appl. Mater. Interfaces* **2021**, *13*, 12211–12220.

[15] Chargui, T.; Lmai, F.; Rahmani, K. Optimization of CZTSSe solar cells by defect analysis and control to reduce recombination with WS_2 non-toxic buffer layer and BSF structures. *Sol. Energy Mater. Sol. Cells* **2025**, *282*, 113424.

[16] Xu, H. Y.; Cong, Y. J.; Qin, S. M.; Guo, X. Y.; Gao, H. F.; Gao, Z. R.; Wang, X. Z.; Sun, Y. L.; Gao, C.; Dai, W. L. et al. Improving back interface quality and passivating defects of $Cu_2ZnSnSe_4$ solar cells via introducing a hydrogen plasma treated intermediate layer. *J. Alloys Compd.* **2025**, *1011*, 178306.

[17] Dimitrievska, M.; Giraldo, S.; Pistor, P.; Saucedo, E.; Pérez-Rodríguez, A.; Izquierdo-Roca, V. Raman scattering analysis of the surface chemistry of kesterites: Impact of post-deposition annealing and Cu/Zn reordering on solar cell performance. *Sol. Energy Mater. Sol. Cells* **2016**, *157*, 462–467.

[18] Yan, C.; Huang, J. L.; Sun, K. W.; Johnston, S.; Zhang, Y. F.; Sun, H.; Pu, A. B.; He, M. R.; Liu, F. Y.; Eder, K. et al. Cu_2ZnSnS_4 solar cells with over 10% power conversion efficiency enabled by heterojunction heat treatment. *Nat. Energy* **2018**, *3*, 764–772.

[19] Su, Z. H.; Liang, G. X.; Fan, P.; Luo, J. T.; Zheng, Z. H.; Xie, Z. G.; Wang, W.; Chen, S.; Hu, J. G.; Wei, Y. D. et al. Device postannealing enabling over 12% efficient solution-processed Cu_2ZnSnS_4 solar cells with Cd^{2+} substitution. *Adv. Mater.* **2020**, *32*, 2000121.

[20] Kim, S.; Lee, J.; Son, D. H.; Kim, W. H.; Sung, S. J.; Hwang, D. K.; Hong, T. E.; Otgontamir, N.; Enkhbayar, E.; Lee, T. H. et al. Reducing carrier recombination loss by suppressing Sn loss and defect formation via Ag doping in $Cu_2ZnSn(S,Se)_4$ solar cells. *Energy Environ. Sci.* **2024**, *17*, 8609–8620.

[21] Wang, Y. T.; Guo, J. Y.; Siqin, L.; Yang, C. J.; Wang, L.; Li, S. Y.; Liu, R. J.; Luan, H. M.; Zhu, C. J. Enhancing the photovoltaic efficiency of CZTSSe thin-film solar cells via Ag-doping induced defect modulation. *Sol. Energy Mater. Sol. Cells* **2024**, *277*, 113138.

[22] Guo, X. C.; Cui, X. P.; Sun, K.; Luo, X. Y.; Zhou, W. H.; Kou, D. X.; Wu, S. X. Ag,Cd double gradient doping at front interface for high efficiency CZTSSe solar cells. *Chem. Eng. J.* **2025**, *503*, 158123.

[23] Li, M. G.; Ma, D.; Wang, C. K.; Wang, T.; Yao, B.; Li, Y. F.; Ding, Z. H.; Sun, Y. T.; Sun, X. F.; Zhu, Y. et al. Enhancing performance of $Cu_2ZnSn(S,Se)_4$ solar cells via non-uniform gradient and flat bands induced by Cd substitution. *Sol. Energy* **2024**, *283*, 113063.

[24] Xiang, S. T.; Li, Y. Z.; Xiang, C. X.; Liu, H. K.; Zheng, Y. Y.; Wang, S. Y.; Yan, W. B.; Xin, H. Improving the performance of kesterite solar cells by solution germanium alloying. *Phys. Chem. Chem. Phys.* **2024**, *26*, 20645–20652.

[25] Guo, R.; Li, X.; Jiang, Y. H.; Zhou, T. X.; Xia, Y. M.; Wang, P.; Liang, Y.; Sui, Y. R.; Yao, B.; Liu, Y. Regulating Sn_{Zn} defects and optimizing bandgap in the $Cu_2ZnSn(S,Se)_4$ absorption layer by Ge gradient doping for efficient kesterite solar cells. *Ceram. Int.* **2024**, *50*, 18329–18336.

[26] Cong, J. L.; He, M. R.; Jang, J. S.; Huang, J. L.; Privat, K.; Chen, Y. S.; Li, J. J.; Yang, L. M.; Green, M. A.; Kim, J. H. et al. Unveiling the role of Ge in CZTSSe solar cells by advanced micro-to-atom scale characterizations. *Adv. Sci.* **2024**, *11*, 2305938.

[27] Sun, Q. Z.; Shi, C.; Xie, W. H.; Li, Y. F.; Zhang, C. X.; Wu, J. H.;

Zheng, Q.; Deng, H.; Cheng, S. Y. Defect synergistic regulations of Li&Na co-doped flexible $Cu_2ZnSn(S,Se)_4$ solar cells achieving over 10% certified efficiency. *Adv. Sci.* **2024**, *11*, 2306740.

[28] Zhong, X. Y.; Wang, J. L.; Han, L. T.; Chi, J. J.; Liu, T.; Kou, D. X.; Zhou, W. H.; Zhou, Z. J.; Yuan, S. J.; Meng, Y. N. et al. Li,Ag co-doping enables efficient kesterite solar cell with a high fill factor of 74.30%. *Adv. Funct. Mater*., in press, DOI: 10.1002/adfm.202418548.

[29] Siqin, L. T.; Yang, C. J.; Guo, J. Y.; Wang, Y. T.; Wang, L.; Li, Y.; Wang, Y. M.; Li, S. Y.; Chen, X. Y.; Luan, H. M. et al. Achieving 11.23% efficiency in CZTSSe solar cells via defect control and interface contact optimization. *Sol. Energy* **2024**, *283*, 112913.

[30] Yan, Q.; Sun, Q. Z.; Deng, H.; Xie, W. H.; Zhang, C. X.; Wu, J. H.; Zheng, Q.; Cheng, S. Y. Enhancing carrier transport in flexible CZTSSe solar cells via doping Li strategy. *J. Energy Chem.* **2022**, *75*, 8–15.

[31] Gershon, T.; Lee, Y. S.; Antunez, P.; Mankad, R.; Singh, S.; Bishop, D.; Gunawan, O.; Hopstaken, M.; Haight, R. Photovoltaic materials and devices based on the alloyed kesterite absorber $(Ag_xCu_{1-x})_2ZnSnSe_4$. *Adv. Energy Mater.* **2016**, *6*, 1502468.

[32] Gong, Y. C.; Qiu, R. C.; Niu, C. Y.; Fu, J. J.; Jedlicka, E.; Giridharagopal, R.; Zhu, Q.; Zhou, Y. G.; Yan, W. B.; Yu, S. T. et al. Ag incorporation with controlled grain growth enables 12.5% efficient kesterite solar cell with open circuit voltage reached 64.2% Shockley–Queisser limit. *Adv. Funct. Mater.* **2021**, *31*, 2101927.

[33] Qi, Y. F.; Kou, D. X.; Zhou, W. H.; Zhou, Z. J.; Tian, Q. W.; Meng, Y. N.; Liu, X. S.; Du, Z. L.; Wu, S. X. Engineering of interface band bending and defects elimination via a Ag-graded active layer for efficient $(Cu,Ag)_2ZnSn(S,Se)_4$ solar cells. *Energy Environ. Sci.* **2017**, *10*, 2401–2410.

[34] Zhao, X. Y.; Chang, X. H.; Kou, D. X.; Zhou, W. H.; Zhou, Z. J.; Tian, Q. W.; Yuan, S. J.; Qi, Y. F.; Wu, S. X. Lithium-assisted synergistic engineering of charge transport both in GBs and GI for Ag-substituted $Cu_2ZnSn(S,Se)_4$ solar cells. *J. Energy Chem.* **2020**, *50*, 9–15.

[35] Tong, J. Y.; Wang, S. T.; Wang, G.; Liu, Y.; Wang, Y. X.; Chen, L. P.; Wang, L. L.; Pan, D. C.; Zhang, X. T.; Liu, Y. C. Li^+&Ag^+ and Li^+&Cd^{2+} double-ion-doping strategy to improve the efficiency of $Cu_2ZnSn(S,Se)_4$ solar cells. *Sol. Energy* **2021**, *220*, 882–889.

[36] Liu, Y.; Hu, C. Y.; Qi, Y. F.; Zhou, W. H.; Kou, D. X.; Zhou, Z. J.; Han, L. T.; Meng, Y. N.; Yuan, S. J.; Wu, S. X. Li/Ag co-doping synergistically boosts the efficiency of kesterite solar cells through effective Sn_{Zn} defect passivation. *Adv. Mater. Interfaces* **2022**, *9*, 2201677.

[37] Gong, Y. C.; Jimenez-Arguijo, A.; Medaille, A. G.; Moser, S.; Basak, A.; Scaffidi, R.; Carron, R.; Flandre, D.; Vermang, B.; Giraldo, S. et al. Li-doping and Ag-alloying interplay shows the pathway for kesterite solar cells with efficiency over 14%. *Adv. Funct. Mater.* **2024**, *34*, 2404669.

[38] Liu, Y.; Zhang, H. M.; Meng, R. T.; Dong, J. B.; Xu, X. J.; Zhang, J. C.; Zhang, Y. Tailoring Li assisted CZTSe film growth under controllable selenium partial pressure and solar cells. *J. Chem. Phys.* **2024**, *161*, 124709.

[39] Xiao, H. Q.; Zhou, W. H.; Kou, D. X.; Zhou, Z. J.; Meng, Y. N.; Qi, Y. F.; Yuan, S. J.; Tian, Q. W.; Wu, S. X. Boosting the efficiency of solution-based CZTSSe solar cells by supercritical carbon dioxide treatment. *Green Chem.* **2020**, *22*, 3597–3607.

[40] Guo, H. L.; Meng, R. T.; Hu, L.; Lin, C. H.; Sun, Y. L.; Liu, Y.; Wu, J. Y.; Shen, Z.; Chu, D. W.; Wang, G. et al. Optimization of the selenization pressure enabling efficient $Cu_2ZnSn(S,Se)_4$ solar cells. *Sol. RRL* **2022**, *6*, 2100778.

[41] Zhou, J. Z.; Xu, X.; Duan, B. W.; Wu, H. J.; Shi, J. J.; Luo, Y. H.; Li, D. M.; Meng, Q. B. Regulating crystal growth via organic lithium salt additive for efficient kesterite solar cells. *Nano Energy* **2021**, *89*, 106405.

[42] Kim, S. Y.; Son, D. H.; Kim, Y. I.; Kim, S. H.; Kim, S.; Ahn, K.; Sung, S. J.; Hwang, D. K.; Yang, K. J.; Kang, J. K. et al. Void and secondary phase formation mechanisms of CZTSSe using Sn/Cu/Zn/Mo stacked elemental precursors. *Nano Energy* **2019**, *59*, 399–411.

[43] Son, D. H.; Kim, D. H.; Park, S. N.; Yang, K. J.; Nam, D.; Cheong, H.; Kang, J. K. Growth and device characteristics of CZTSSe thin-film solar cells with 8.03% efficiency. *Chem. Mater.* **2015**, *27*, 5180–5188.

[44] Sun, Y. X.; Zhang, Y. Z.; Wang, H.; Xie, M.; Zong, K.; Zheng, H. J.; Shu, Y. Q.; Liu, J. B.; Yan, H.; Zhu, M. K. et al. Novel non-hydrazine solution processing of earth-abundant $Cu_2ZnSn(S,Se)_4$ absorbers for thin-film solar cells. *J. Mater. Chem. A* **2013**, *1*, 6880–6887.

[45] Meng, R. T.; Xu, X. J.; Huang, Y.; Wu, L.; Li, J. P.; Xu, H.; Dong, J. B.; Liu, Y.; Fu, X. W.; Guo, H. L. et al. Reversing band bending at grain boundaries enables high-efficiency $Cu_2ZnSn(S,Se)_4$ solar cells. *Mater. Today Phys.* **2024**, *48*, 101580.

[46] Xu, H.; Meng, R. T.; Xu, X. J.; Wu, L.; Sun, Y. L.; Liu, Y.; Wang, Z. Y.; Wang, N.; Li, M.; Zhang, Y. Facile tailor on the surface of Mo foil toward high-efficient flexible CZTSSe solar cells. *Small Methods* **2024**, *9*, 2401084.